LA-UR-81-1404

TITLE: TEMPORAL SHAPING OF NANOSECOND CO_2 LASER PULSES IN MULTIPHOTON SATURABLE ABSORBERS

AUTHOR(S): Richard F. Haglund, Jr, P-1

MASTER

SUBMITTED TO: Proceedings of the Los Alamos Conference on Optics '81
Santa Fe, NM April 6-10, 1981

University of California

DISCLAIMER

By acceptance of this article, the publisher recognizes that the U.S. Government retains a nonexclusive, royalty-free license to publish or reproduce the published form of this contribution, or to allow others to do so, for U.S. Government purposes

The Los Alamos Scientific Laboratory requests that the publisher identify this article as work performed under the auspices of the U.S. Department of Energy

LOS ALAMOS SCIENTIFIC LABORATORY
Post Office Box 1663 Los Alamos, New Mexico 87545
An Affirmative Action/Equal Opportunity Employer

Form No. 836 R3
St. No. 2629
12/78

UNITED STATES
DEPARTMENT OF ENERGY
CONTRACT W-7405-ENG 36

DISTRIBUTION OF THIS DOCUMENT IS UNLIMITED

TEMPORAL SHAPING OF NANOSECOND CO_2 LASER PULSES IN MULTIPHOTON SATURABLE ABSORBERS

R. F. Haglund, Jr.
University of California
Los Alamos National Laboratory
Los Alamos, NM 87545

The power amplifiers used in the Helios CO_2 fusion laser[1] are stabilized against parasitic oscillations[2] by the use of SF_6-based gaseous saturable absorbers.[3] The single absorber cell in the Helios power amplifier chain is located so that it provides gain isolation between the preamplifiers and the first pass through the power amplifier, as well as between the second and third passes through the power amplifier. Hence, the absorber loss characteristics cannot easily be optimized to match the fluence and intensity levels characteristics of each successive stage of amplification. This in turn, creates the possibility of nonlinear pulse-shaping effects in the absorbing medium.

In a recent paper,[4] Nowak and Ham have reported severe spatial pulse distortion for nanosecond CO_2 laser pulses traversing SF_6 gas samples at modest pressure-length products. Preliminary experiments showed no spatial effects in the Helios saturable absorber mixtures. However, motivated by this discovery of nonlinear index effects in SF_6, we have looked for and found substantial temporal pulse distortion both in SF_6 and in the SF_6-based fluorocarbon gas isolator, Mix 907, used for parasitic suppression in the Helios laser. The observed effects which are of most concern in an operating fusion laser system are (1) a wavelength- and fluence-dependent increase in pulse risetime; and (2) a wavelength-dependent dispersion in the transit time of a nanosecond laser pulse through the absorbing medium. Both of these

effects are undesirable in current CO_2 fusion laser systems, which use multiwavelength pulses to maximize energy extraction and which must have the fastest possible risetimes.

In the following paper, we first describe our experiments and present representative data. We then show that temporal pulse shaping occurs even in a simple two-level absorber model. Finally, we discuss the applicability of this model to multiphoton absorbers, such as SF_6 and Mix 907 and consequences of our observations for practical system design.

I. Experimental Layout

The laser used for the experiment has been described in detail elsewhere.[5] It consists of a grating-controlled hybrid TEA oscillator and a double-passed TEA amplifier. The oscillator produces a temporally smooth 120-ns pulse, and can be tuned throughout the 9.4-μm and 10.4-μm bands of the CO_2 laser spectrum, between the oscillator and amplifier as a two-stage CdTe electrooptic switch, which is driven by a laser-triggered spark gap. This CdTe Pockels cell switches out a 1.7-ns (FWHM) slice of the oscillator pulse before it makes its first pass through the amplifer. The amplifier output is compressed by a reflecting telescope and then spatially filtered to produce a beam with a smooth Gaussian spatial profile. The beam is weakly focused before entering the screen room housing the experiment by a 20-m concave mirror. In the screen room, it has a radius at 1/e of peak intensity of about 3.5 mm, and a peak energy of about 300 mJ. Measurements with a 128-element pyroelectric array (interelement spacing 1 mm) confirm that the spatial profile of the beam is constant over the length of the gas sample cell used. The temporal pulse shape is roughly triangular, with a 10 - 90% risetime of 450 ps, a fall time of 1750 ps, and a width (FWHM) of 1700 ps.

The experimental arrangement is shown in Fig. 1. The gas cell used for the pulse-shape measurements is 19.8 cm in length, and is sealed by NaCl windows mounted at Brewster's angle. The body of the gas cell is made of Pyrex to insure that the fluorocarbon gases do not react with the cell walls. The cell is filled and evacuated through a manifold of conventional design, connected to various small gas cylinders and to an air-cooled diffusion pump. Gases used were of standard chemical purity. Pressures are monitored by means of differential capacitance manometers.

The incident fluence on the cell is controlled by putting calibrated CaF_2 attenuators in front of the entrance window of the gas cell. The signal incident on the pyroelectric detector at the cell exit is kept to reasonable limits by keeping the <u>total</u> attenuation before and after the cell constant. The values of the attenuators in the stack are chosen to give appropriate fluence increments (typically two points per decade) from 0.01 to 1000 mJ/cm^2.

A pair of compensated salt wedges is used to split off a portion of the incident beam for diagnostic purposes. This diagnostic beam is further split using a single NaCl wedge, and the two beams are then directed into fast and slow pyroelectric detectors to measure pulse shape and incident energy, respectively. A second fast pyroelectric detector is used to measure the pulse shape at the end of the gas cell. The output signals from the fast pyroelectric detectors are delayed with respect to one another so that the signals can be added at the input of a 5-GHz oscilloscope and appear on the same trace. The risetime of the fast pyroelectric detector is ~ 80 ps, which is negligible compared to the characteristic time scales of the laser pulses.

The fluorocarbon absorber Mix 907 used in these experiments has been extensively characterized elsewhere.[3] Its composition is given in Table I below. The "FC" designator refers to the standard fluorocarbon numbering system of the American Chemical Society.

Table I: Composition of Mix 907

Gas	Mole Fraction
Sulfur Hexafluoride	0.0089
Perfluorocyclobutane (FC-318a)	0.0227
Chloropentafluoroethane (FC-115)	0.0664
1,1-Difluoroethane (FC-152a)	0.0909
1,1-Dichloro - 2,2-difluoroethylene	0.1363
Dichlorodifluoromethane (FC-12)	0.2500
Chlorotrifluoroethylene (FC-1113)	0.4255

The raw data produced in the experiment are the incident energies (as monitored by the detector labelled SPD in Fig. 1) and the oscilloscope traces produced by the fast pyroelectric detectors which monitor the pulse shape immediately before and after the gas cell.

The energy scale for the pyroelectric joulemeter was determined by inserting a Scientech disk calorimeter in place of the gas cell (see Fig. 1). Once this calibration was made, all energies read by the joulemeter are correlated with the energy incident on the CaF_2 attenuator stack efore the gas cell. The energy incident on the gas sample was calculated by including the effects of the CaF_2 attenuators and the salt entrance window on the incident beam. Subsequent measurements indicated that the scale error in the energy calculated in thi way may be as much as 15%.

The pulse traces from the 5-GHz oscilloscope were digitized using a plotting board with 0.25 mm resolution, connected to an HP-9845A computer and graphics terminal. Sweep nonlinearities in the oscilloscope were taken into account by digitizing (on the same plotting board) the trace from a 1-GHz oscillator fed into the 5-GHz oscilloscope. The nonlinearity can be fitted by a linear function of the sweep time. The digitizing program calculates various pulse parameters, such as risetime, falltime, pulse width (FWHM) and time delay between the leading edges (at 50% of peak amplitude), peak, and trailing edges of the incident and exit pulses. Repeated digitizations of the same pulses indicate that the accuracy of the digitization process is about ± 10% for the risetime, ± 5% for falltimes, and ± 5% for pulse widths and interpulse delay times.

II. Experimental Observations

The present experiment was intended as a survey, to see what kind of pulse-shaping behavior was observed and how this behavior depended on fluence and laser frequency. The results shown in Figs. 2, 3 and 4 and the summary in Table II are culled from some two hundred shots through samples of both SF_6 and Mix 907.

Figure 2 shows a comparison of pulse shapes for the input and output pulses with the gas cell evacuated. The 10 - 90% risetime for the incident pulse is typically 400 - 450 ps. Differences in risetime ratios (incident pulse risetime/exit pulse risetime) of less than 0.1 are not considered significant in this time scale. The vacuum risetime ratio calculated directly from the digitized oscilloscope trace is not unity because of the pronounced nonlinearity in the sweep.

The pulse traces shown in Fig. 3 are for a 1.7-ns laser pulse incident on 60 torr-cm of SF_6, at a peak fluence of approximately 600 mJ/cm^2. If one normalizes the risetime ratios for these pulses to that for the vacuum, one obtains the result that the pulse risetime in SF_6 is lengthened from ~ 450 ps to ~ 600 ps. Similar results are obtained at other frequencies (see Table II). The data given in Table II were all taken with 60 torr-cm SF_6 in the gas cell. Risetime ratios are normalized to the average vacuum risetime (about 1.43). Peak incident fluence in each case is approximately 600 mJ/cm^2. At low fluences (~60 mJ/cm^2), the risetime ratios remained constant, while the peak delay time increased by 5 - 8%.

Table II: Wavelength Dependence of Pulse Shape

Wavelength	Normalized Risetime Ratio	Peak Delay	Gas
10.6 μm P(20)	1.0	580	Vacuum
10.6 μm P(14)	1.0	610	60 torr-cm SF_6
10.6 μm P(20)	1.3	640	60 torr-cm SF_6
10.6 μm P(24)	1.3	630	60 torr-cm SF_6

The pulse delays idicated in Table II are simply the time interval between incident and exit pulse peaks. The change in delay between high-fluence and low-fluence exit pulses is primarily due to the fact that, in the low-fluence case, a greater fraction of the leading edge of the pulse is absorbed as the gas saturates. This kind of behavior is reproduced qualitatively by the simple model discussed in Section III below.

Figure 4 shows the fluence dependence of the risetime ratio for 10 torr-cm of pure SF_6 and for 800-torr-cm of Mix 907. The data fall reasonably well on the best-fit straight line. The experimental errors - on the order of ± 0.15 in the risetime ratio - do not justify a more sophisticated fitting procedure. Since the mole fraction of SF_6 is nearly identical in the two cases, we conclude that the risetime degradation is determined primarily by the pressure-length product of the SF_6. It should be noted that the pulse-shaping is not negligible even at moderately high fluences. In particular, since absorber pressure-length products in Helios are of order 2500 torr-cm, the effects are likely to be observable even above 50 mJ/cm^2.

III. Pulse-Shape Modeling

Because the risetime degradation of nanosecond pulses at high fluences is not what one normally expects of a saturable absorber, we attempted some parameter space scans with a simple model calculation to see if such behavior could be observed experimentally.

We used the model of Frantz and Nodvik,[6] because it is expressible analytically in terms of parameters which have some readily apparent physical significance. In this model, the pulse intensity at time after passing through a saturable absorber with total small-signal loss α and saturation energy E_{sat} is given by

$$I(t) = \frac{I_0(t)}{1 - [1-\exp(\alpha)]\exp[-E_0(t)/E_{sat}]} \qquad (1)$$

where $I_0(t)$ is the input pulse intensity and the integrated energy $E_0(t)$ is

$$E_0(t) = \int_0^t I_0(\tau)d\tau \qquad (2)$$

The loss α and saturation energy E_{sat} are expressible as

$$\alpha = \sigma(\omega)N_0 \qquad (3)$$

$$E_{sat} = \frac{\hbar\omega}{2\sigma(\omega)}$$

where $\sigma(\omega)$ is the absorption cross section and N_0 is the inversion density. In this model, one is dealing only with a two-level system, and neither spontaneous emission nor linewidth effects are accounted for.

Figure 5 shows how a Frantz-Nodvik absorber (solid curve) compares to an ideal saturable absorber (dashed curve) and to MIx 907. The multiphoton absorber, Mix 907, goes into saturation sooner, but takes three decades in fluence to saturate, and even then it fails to saturate completely. Hence we should not expect to see detailed quantitative agreement between the simple model and the behavior of pulses passing through a multiphoton absorber such as SF_6.

Figure 6 shows the triangular pulse used as input in all the calculations, while Figs. 7, 8 and 9 show the output pulse shapes computed from Eq. 1. Figure 7 indicates that the loss α has little effect on the pulse shape by itself, since increasing a by a factor of three only results in a loss of slightly more of the leading edge of the pulse. From Figs. 8 and 9, on the other hand, it is apparent that the ratio of the incident pulse energy to the saturation energy is crucial to the temporal behavior of the pulse. It would appear that for $E_{sat} > 0.05\ E_{inc}$, one can expect significant risetime effects.

The situation depicted in Figs. 8 and 9 is in the range of physical parameters encountered in operating high-gain CO_2 laser systems. Small-signal losses are high, typically of order 15 to 20. In the sense of

the Frantz-Nodvik model, one cannot easily say what E_{sat} is for a multiphoton absorber, but it is clearly much greater than the energy at which the absorber first begins to bleach. An effective saturation energy of several millijoules seems a reasonable number to assign, especially in view of the nonsaturable loss which the multiphoton absorber experiences. In this regime, it is evident that even a simple two-level absorption model predicts pulse-shaping effects which are qualitatively similar to experimental observations.

Figure 10 shows one difficulty which arises when a multiwavelength pulse is propagated through a Frantz-Nodvik absorber. Here we have used a saturation energy of five millijoules, and the input pulse is the same as that displayed in Fig. 6. The loss α is varied to correspond to the values of α experienced by 10.6 μm P(16), P(18) and P(20) pulses passing through 60 torr-cm SF_6. It is evident that the peak of the P(16) pulse is delayed almost 300 ps with respect to the P(20) pulse. This implies that multiwavelength pulses will be "stretched" in passing through a saturable absorber, by a delay time related to the attenuation. Qualitatively similar results appear in Table II, where the pulse delays for P(14) and P(24) are less than for P(20), which experiences a greater attenuation than either of the other two lines. Moreover, the stretching effect will be exacerbated in any amplification process occurring after the saturable absorber. Hence, for a given pulse energy, a multiwavelength pulse will have reduced peak power after traversing a saturable absorber when compared to a monochromatic pulse of the same initial energy and time history.

IV. Conclusions

We have shown that substantial temporal distortion of nanosecond 10.6 μm laser pulses occurs in traversing multiphoton saturable absorbers. The risetime and pulse delay effects appear to depend both on fluence and wavelength, and to be qualitatively consistent with predictions of a simple two-level absorption model.

These observations have important consequences for the design of practical short-pulse CO_2 laser systems. First, they suggest that pulse-shaping effects can only be minimized, and that a fluence of several hundred mJ/cm^2 is necessary to achieve this minimization. Second, they imply that one should perhaps reexamine the utility of multifrequency energy extraction schemes, since the varying risetime effects and the frequency-dependent dispersion experienced by the pulse in passing through the absorber may reduce peak intensity sufficiently to nullify the gains in energy-extraction efficiency accruing from multifrequency operation of the laser amplifiers.

Further experimental and theoretical work is also indicated. In particular, the fluence and pressure dependence of the pulse shaping needs to be explored. On the theoretical side, the use of a Frantz-Nodvik model with a nonsaturating loss is planned in hopes of obtaining a quantitatively correct description of pulse shaping in multiphoton saturable absorbers.

References

1. R. L. Carlson, J. P. Carpenter, D. E. Casperson, R. B. Gibson, R. P. Godwin, R. F. Haglund, Jr., J. A. Hanlon, E. L. Jolly and T. F. Stratton, "Helios: A 15-TW CO_2 Laser Fusion Facility," J. Quant. Electron., to be published 1981.

2. C. J. Elliott, "Parasitic Oscillations in the Static, Centered Two-Aperture Limit," Appl. Opt., Vol. 19, pp. 2109-2117, 1980.

3. R. F. Haglund, Jr., A. V. Nowak and S. J. Czuchlewski, "Gaseous Saturable Absorbers for the Helios CO_2 Laser System," J. Quant. Electron., to be published 1981.

4. A. V. Nowak and D. O. Ham, "Self-Focusing of 10-μm Laser Pulses in SF_6," Opt. Lett., Vol. 6, pp. 185-187, 1981.

5. J. F. Figueira and A. V. Nowak, "Carbon-Dioxide Laser System with Zero Small-Signal Gain," Appl. Opt., Vol. 19, pp. 420-421, 1980.

6. L. M. Frantz and J. S. Nodvik, "Theory of Pulse Propagation in a Laser Amplifier," J. Appl. Phys., Vol. 34, pp. 2346-2349, 1963.

Figure Captions

1. Experimental layout for pulse-shape measurements. The laser pulse is incident from the lower right. Wedges of NaCl are used to provide diagnostic pick-offs. The labels "SPD" and "FPD" refer respectively to slow and fast pyroelectric detectors.

2. Oscilloscope trace showing input (left) and exit (right) pulse shapes for a 10.6=μm P(20) pulse traversing the evacuated gas cell. The horizontal scale is 1 ns/div.

3. Oscilloscope trace showing input (left) and exit (right) pulse shapes for a 10.6-μm P(20) pulse traversing the gas cell when it contains 3.0 torr of SF_6. Incident peak fluence is approximately 600 mJ/cm^2.

4. Risetime ratio of pulses traversing a gas cell containing 10 torr-cm of SF_6 or 800 torr-cm of Mix 907, as a function of fluence. The pulse wavelength is 10.6-μm P(20).

5. Comparison of the transmission behavior of an ideal saturable absorber with a saturation energy of 1 mJ (dashed curve), a Frantz-Nodvik absorber (solid curve) with small-signal loss of 2 and saturation energy 1 mJ, and a multiphoton saturable absorber (Mix 907) with a small-signal loss of 2.

6. Input pulse used for Frantz-Nodvik calculations.

7. Frantz-Nodvik calculation of pulse shapes (intensity vs time) following transmission through an absorber of varying losses α.

8. Frantz-Nodvik calculation of pulse shapes for transmission through an absorber with varying saturation energy E_{sat} for a fixed incident energy E_{inc} and loss α.

9. Frantz-Nodvik calculation of pulse shapes for transmission through an absorber with a fixed saturation energy E_{sat} and fixed loss α, for varying incident energy E_{inc}.

10. Pulse shapes for 10.6 μm laser lines of different wavelengths in the vicinity of the absorption peak in SF_6. Loss coefficients α are shown corresponding to the actual loss in 60 torr-cm of SF_6.

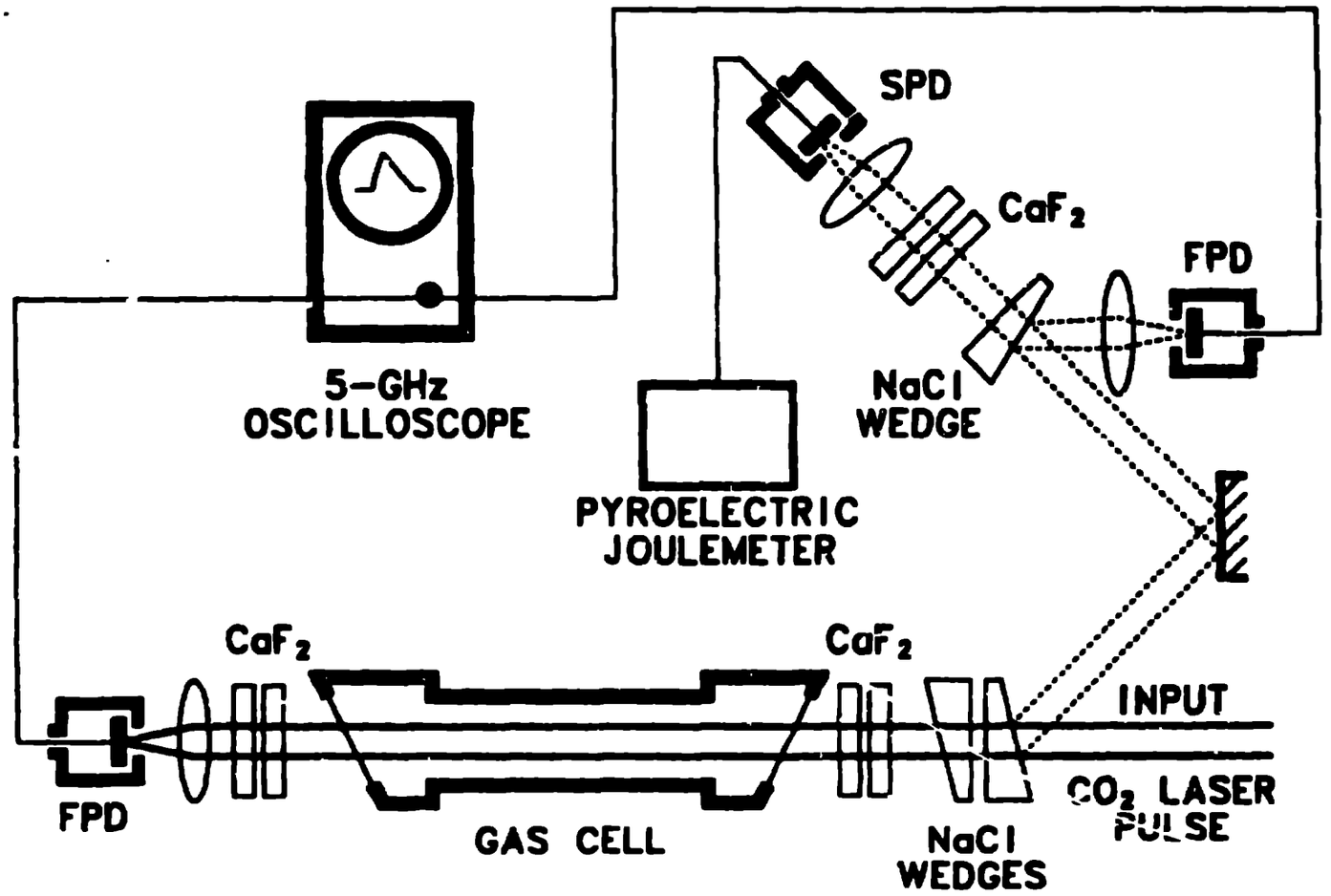
SPD
CaF2
FPD
5-GHz
OSCILLOSCOPE
NaCl
WEDGE
PYROELECTRIC
JOULEMETER
CaF2
CaF2
INPUT
FPD
GAS CELL
NaCl
WEDGES
CO2 LASER
PULSE

FIGURE 1

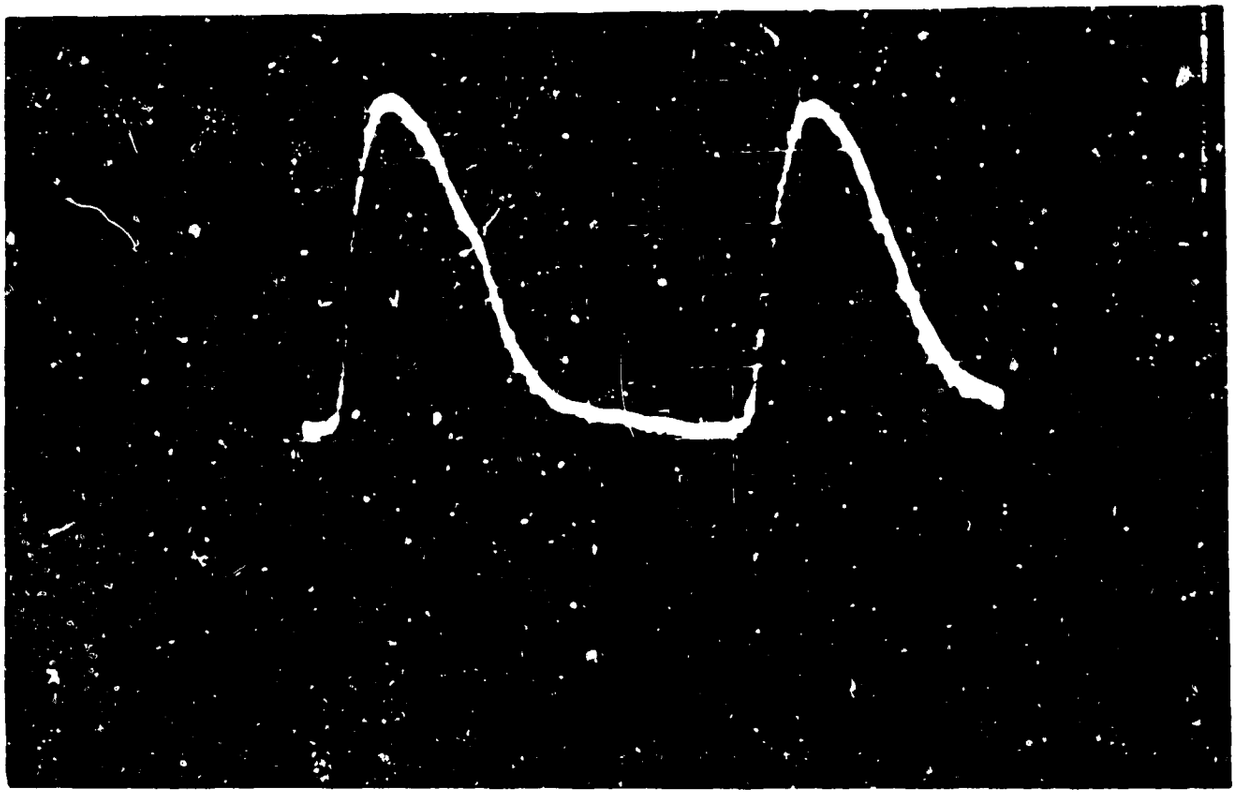

FIGURE 2

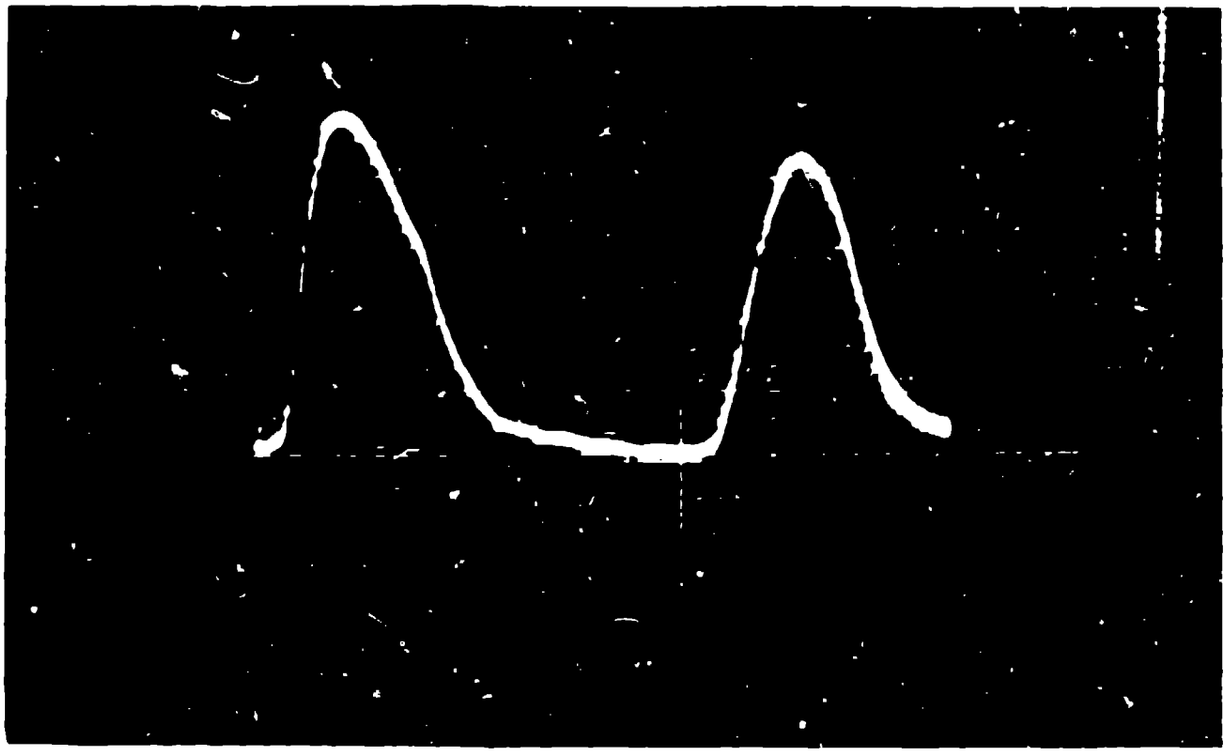

FIGURE 3

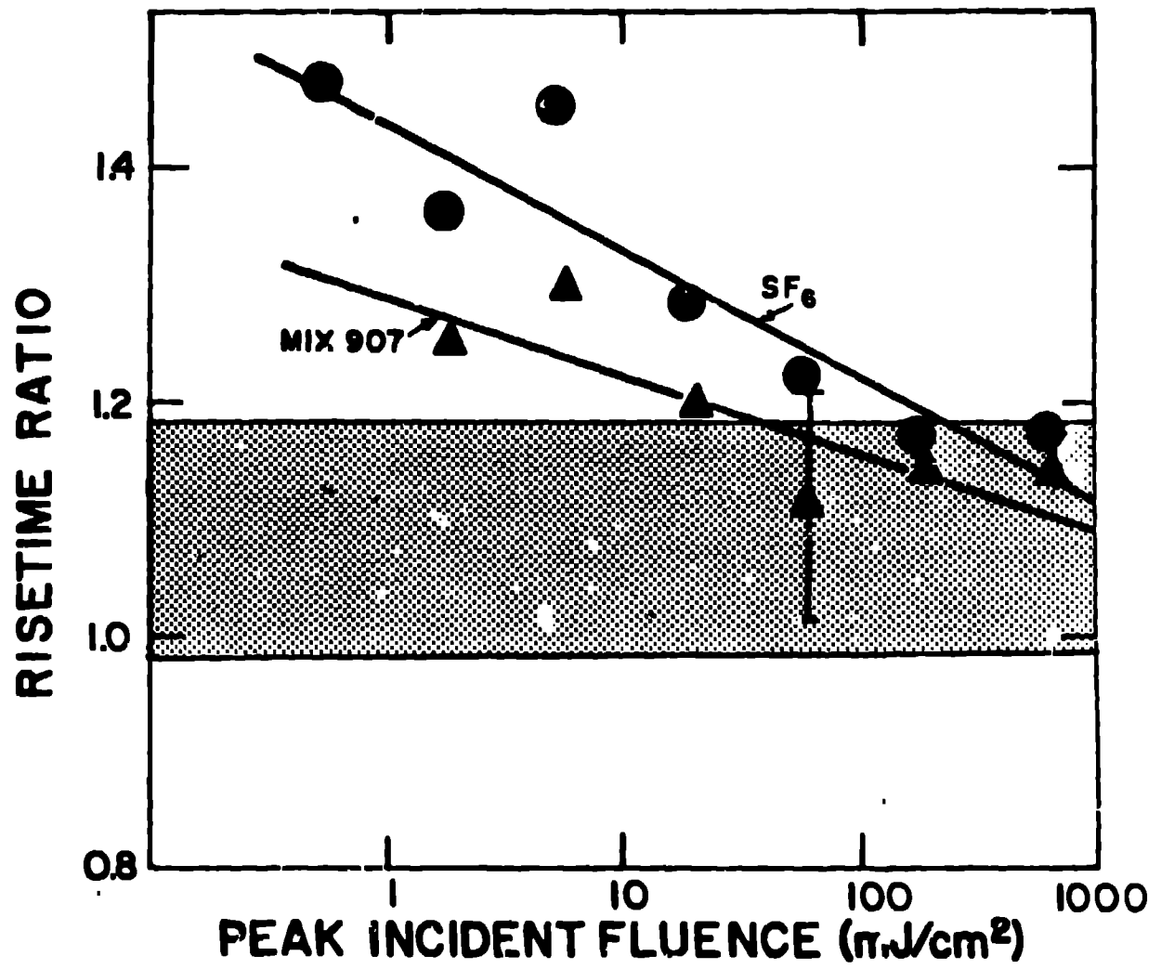
RISETIME RATIO
1.4
1.2
1.0
0.8
SF6
MIX 907
1
10
100
1000
PEAK INCIDENT FLUENCE (mJ/cm2)

FIGURE 4

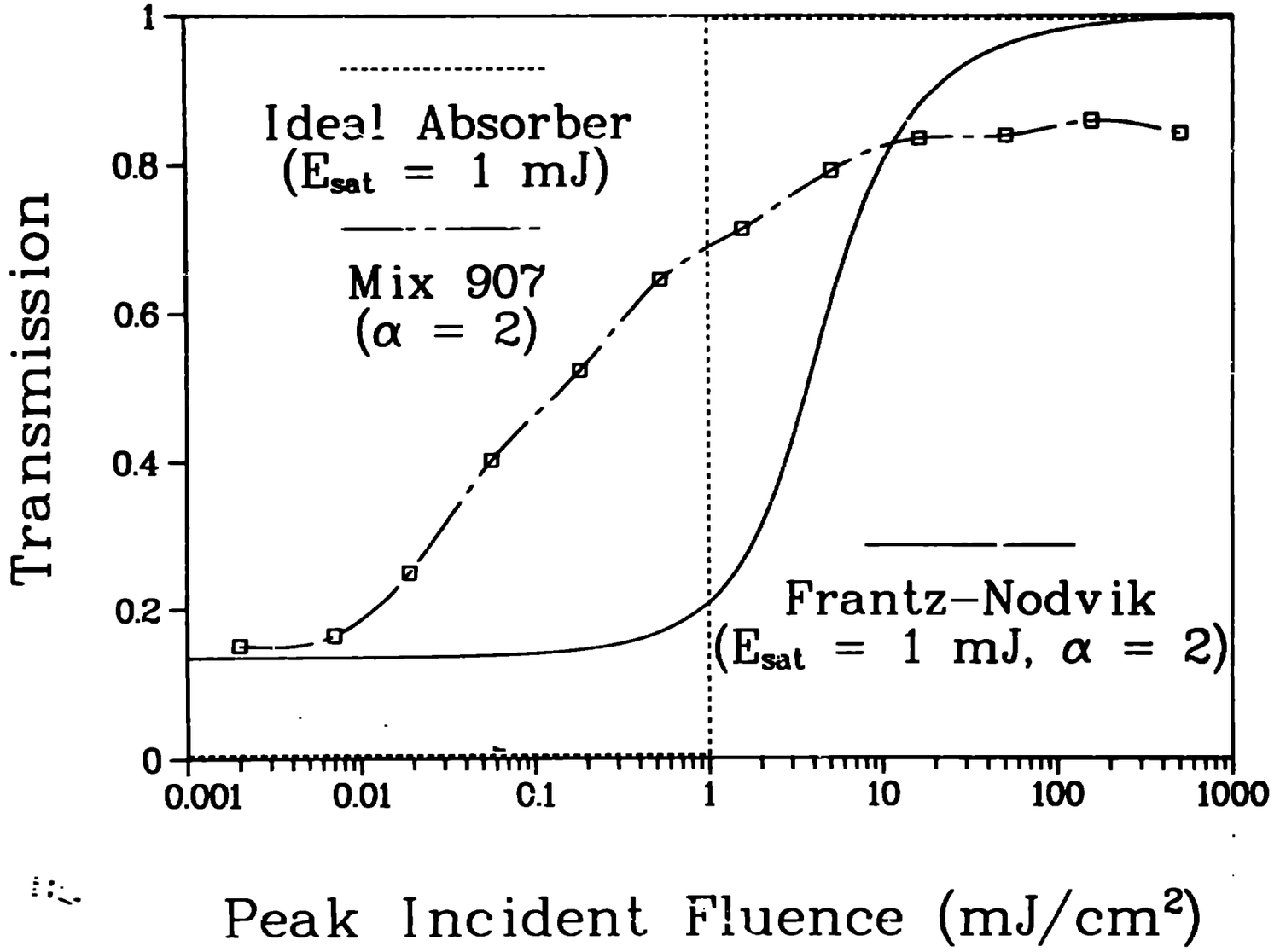
Transmission
1
0.8
0.6
0.4
0.2
0
Ideal Absorber
(E_{sat} = 1 mJ)
Mix 907
(α = 2)
Frantz–Nodvik
(E_{sat} = 1 mJ, α = 2)
0.001
0.01
0.1
1
10
100
1000
Peak Incident Fluence (mJ/cm^2)

FIGURE 5

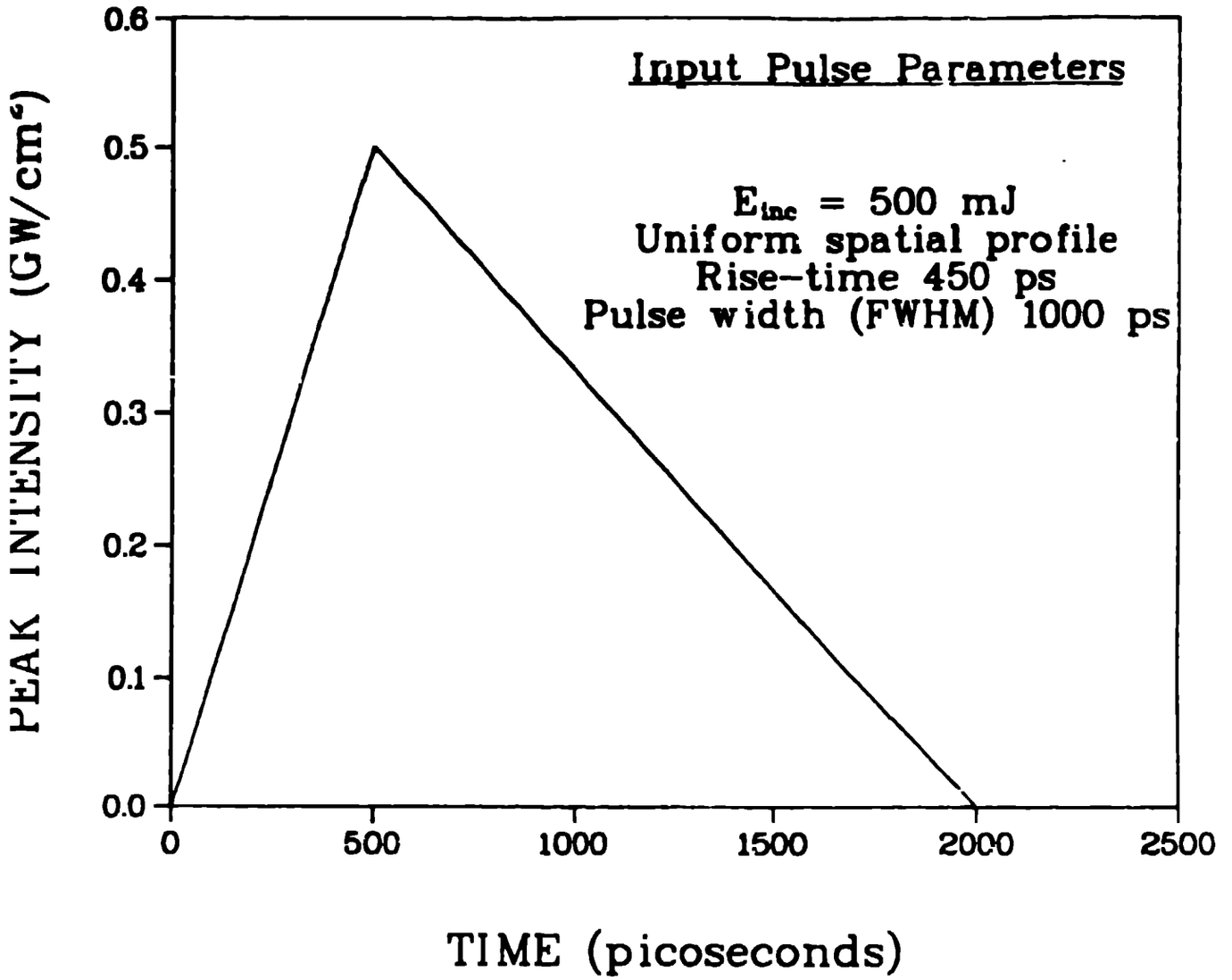
Input Pulse Parameters
E_{inc} = 500 mJ
Uniform spatial profile
Rise-time 450 ps
Pulse width (FWHM) 1000 ps
PEAK INTENSITY (GW/cm²)
0.6
0.5
0.4
0.3
0.2
0.1
0.0
0
500
1000
1500
2000
2500
TIME (picoseconds)

FIGURE 6

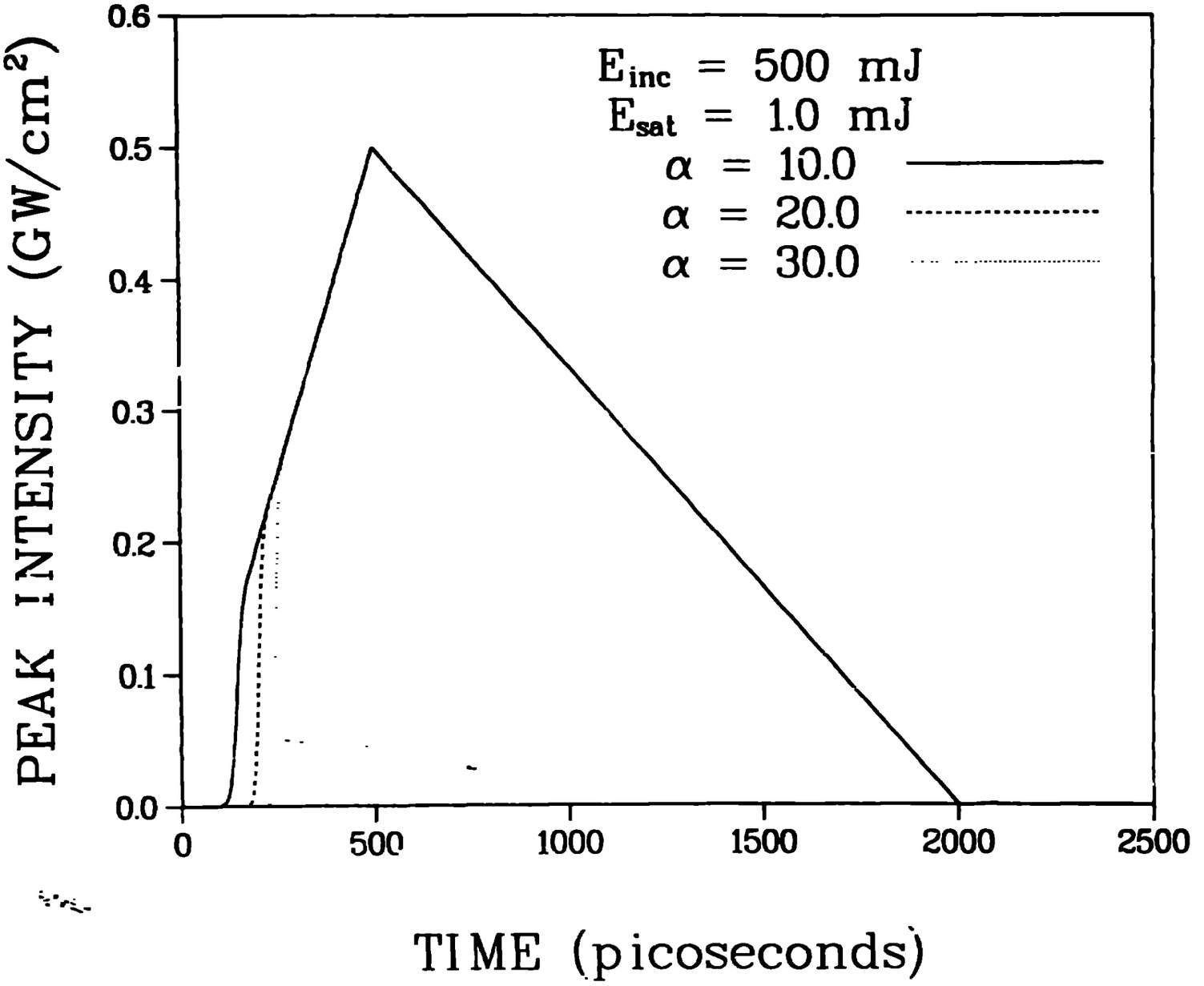
PEAK INTENSITY (GW/cm²)
0.6
0.5
0.4
0.3
0.2
0.1
0.0
0
500
1000
1500
2000
2500
TIME (picoseconds)
E_inc = 500 mJ
E_sat = 1.0 mJ
α = 10.0
α = 20.0
α = 30.0

FIGURE 7

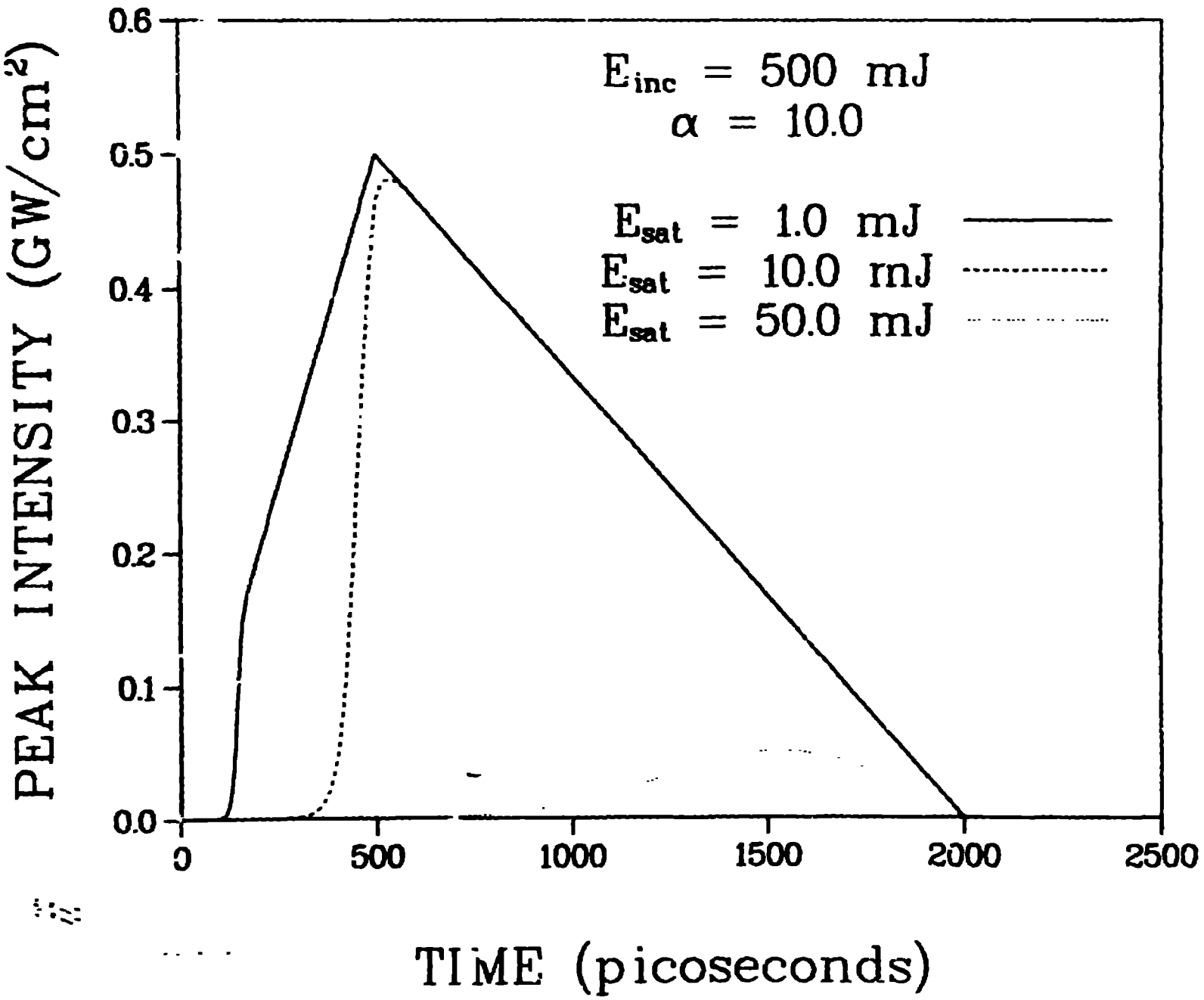
0.6
0.5
0.4
0.3
0.2
0.1
0.0
PEAK INTENSITY (GW/cm²)
E_inc = 500 mJ
α = 10.0
E_sat = 1.0 mJ
E_sat = 10.0 mJ
E_sat = 50.0 mJ
0
500
1000
1500
2000
2500
TIME (picoseconds)

FIGURE 8

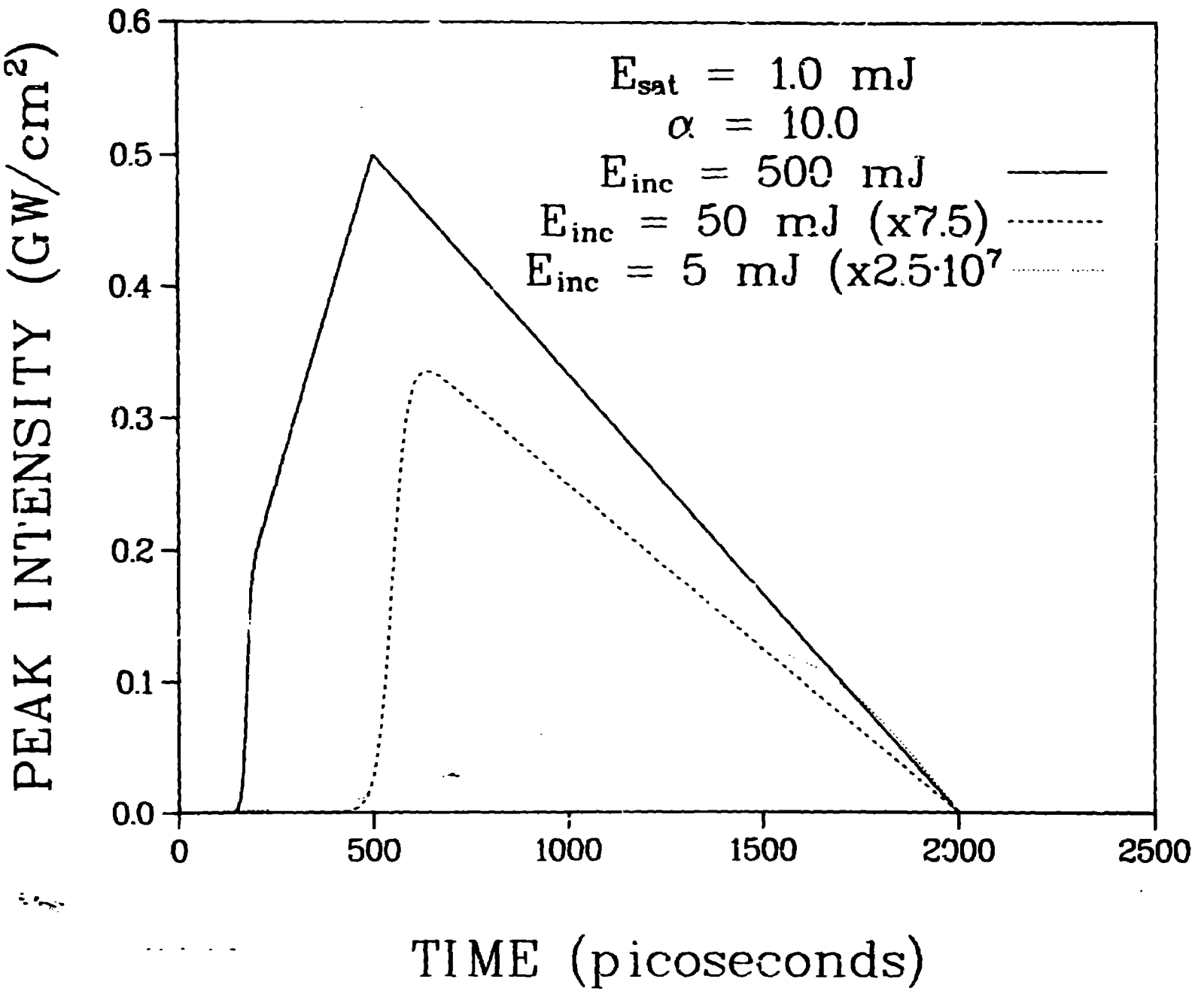
E_{sat} = 1.0 mJ
α = 10.0
E_{inc} = 500 mJ
E_{inc} = 50 mJ (x7.5)
E_{inc} = 5 mJ (x2.5·10^7
PEAK INTENSITY (GW/cm^2)
0.6
0.5
0.4
0.3
0.2
0.1
0.0
0
500
1000
1500
2000
2500
TIME (picoseconds)

FIGURE 9

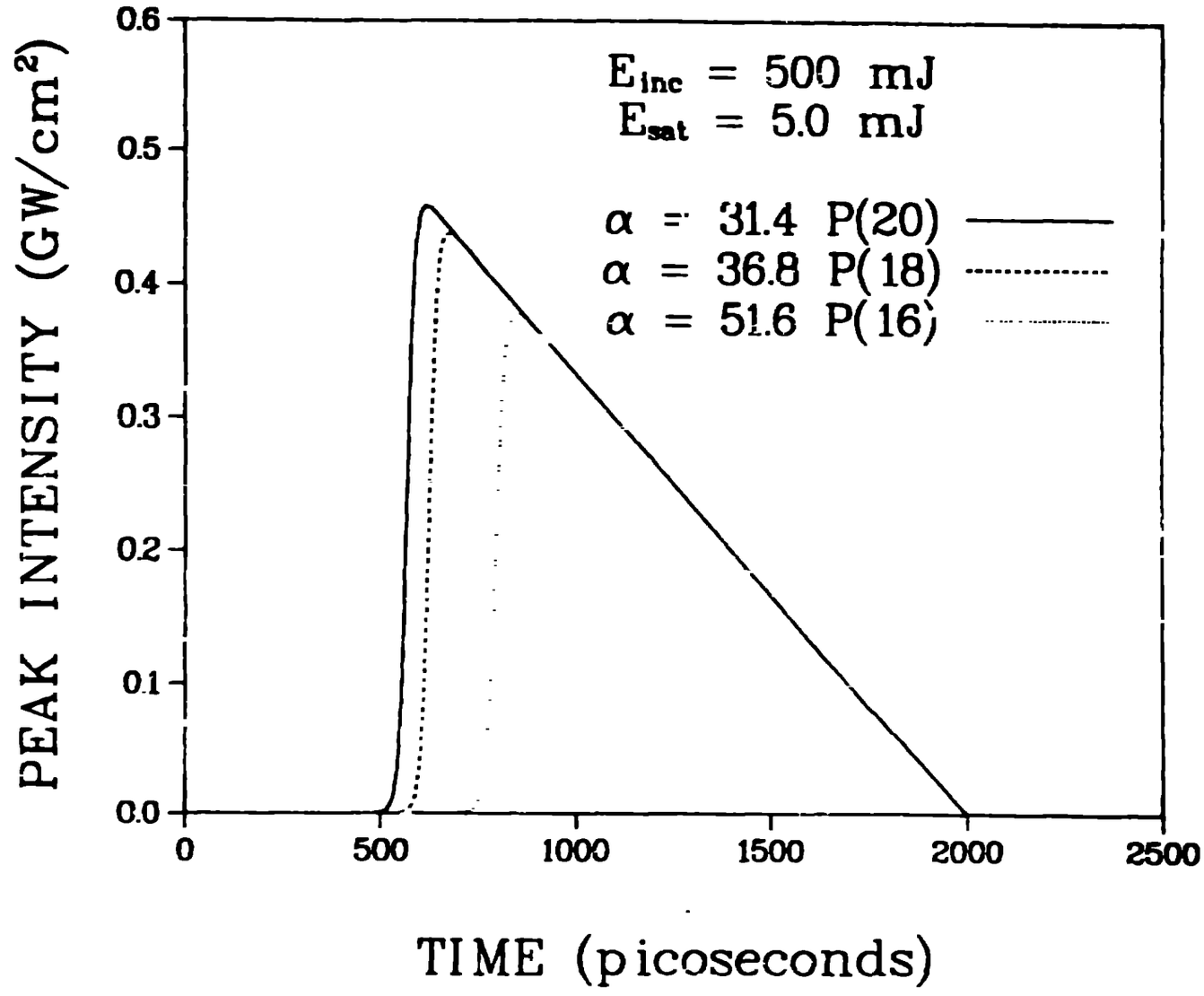
E_{inc} = 500 mJ
E_{sat} = 5.0 mJ
α = 31.4 P(20)
α = 36.8 P(18)
α = 51.6 P(16)
PEAK INTENSITY (GW/cm²)
0.6
0.5
0.4
0.3
0.2
0.1
0.0
0
500
1000
1500
2000
2500
TIME (picoseconds)

FIGURE 10